ANNUAL REVIEWS

Annual Review of Condensed Matter Physics

Topological Magnets: Functions Based on Berry Phase and Multipoles

Satoru Nakatsuji[1,2,3,4] and Ryotaro Arita[5,6]

[1]Department of Physics, University of Tokyo, Hongo, Bunkyo-ku, Tokyo, Japan; email: satoru@phys.s.u-tokyo.ac.jp

[2]Institute for Solid State Physics, University of Tokyo, Kashiwa, Chiba, Japan

[3]Trans-scale Quantum Science Institute, University of Tokyo, Bunkyo-ku, Tokyo, Japan

[4]Institute for Quantum Matter and Department of Physics and Astronomy, Johns Hopkins University, Baltimore, Maryland, USA

[5]Department of Applied Physics, University of Tokyo, Tokyo, Japan

[6]Center for Emergent Matter Science, RIKEN, Saitama, Japan

Annu. Rev. Condens. Matter Phys. 2022. 13:119–42

First published as a Review in Advance on November 4, 2021

The *Annual Review of Condensed Matter Physics* is online at conmatphys.annualreviews.org

https://doi.org/10.1146/annurev-conmatphys-031620-103859

Keywords

Weyl semimetal, antiferromagnetic spintronics, thermoelectric magnet, thermoelectric technology, anomalous Hall effect, anomalous Nernst effect, spin Hall effect, magneto-optical effect

Abstract

Macroscopic responses of magnets are often governed by magnetization and, thus, have been restricted to ferromagnets. However, such responses are strikingly large in the newly developed topological magnets, breaking the conventional scaling with magnetization. Taking the recently discovered antiferromagnetic (AF) Weyl semimetals as a prime example, we highlight the two central ingredients driving the significant macroscopic responses: the Berry curvature enhanced because of nontrivial band topology in momentum space, and the cluster magnetic multipoles in real space. The combination of large Berry curvature and multipoles enables large macroscopic responses such as the anomalous Hall and Nernst effects, the magneto-optical effect, and the novel magnetic spin Hall effect in antiferromagnets with negligible net magnetization, but also allows us to manipulate these effects by electrical means. Furthermore, nodal-point and nodal-line semimetallic states in ferromagnets may provide the strongly enhanced Berry curvature near the Fermi energy, leading to large responses beyond the conventional magnetization scaling. These significant properties and functions of the topological magnets lay the foundation for future technological development such as spintronics and thermoelectric technology.

1. INTRODUCTION

The concept of topology in momentum-space electronic structure has reshaped our understanding of materials properties, driving the discovery of various classes of systems such as topological insulators and nodal-point and nodal-line semimetals (1–3, 5, 6). All these topological materials have been restricted to weakly correlated electron systems, where electronic correlation does not play a major role. Thus, the obvious next step of the research stream is to find novel effects induced primarily by electron correlation. One of the prominent correlation effects is the magnetism, and it is crucial to find novel properties by introducing the notion of topology, e.g., the quantum Berry phase in magnets.

The discovery of such novel quantum phases may enable conceptual advances in material design and engineering, thus serving as a major theme in both basic science and application-related fields. The studies on quantum materials that enable such a revolution in information technology have been rigorously conducted worldwide, because developments in silicon-based technology are slowing down as the semiconductor industry faces the fundamental limit of Moore's law. In the era of global digital transformation using artificial intelligence and trillions of sensors, data traffic and related energy consumption are growing exponentially. For example, analyses suggest that the energy consumption at data centers will reach more than 10% of the total energy used on the globe in a decade. Thus, for global sustainable development, a revolution in materials science is all the more urgent to lay the foundations for information technology that operates at a much faster speed and at much lower power consumption.

Here, we review the rapidly growing field of topological magnets and introduce the key concepts and model materials. In particular, we focus on the quantum mechanical Berry phase effects coming from the nontrivial topology of electronic band structure in momentum space and its coupling to the magnetic structure, including magnetic Weyl semimetals and nodal-line semimetals (4–14). Another class of magnets that exhibits fascinating phenomena are based on (*a*) the topological effects in real space such as magnetic skyrmion materials and geometrically frustrated magnets (15–20) and (*b*) the strong spin-orbit coupling in 4*d* and 5*d* systems and heavy fermion systems (21–24). However, due to space limitations, we exclude these latter classes (*a*) and (*b*) from our review. The number of research reports on topological magnets is increasing exponentially since the initial theoretical proposals and experimental realizations (4, 6–14, 25–27), and thus it is impossible to go over all the materials in this review. Instead, we first cover the general properties of topological magnets. A hallmark of such properties is the anomalous Hall effect (AHE) in an antiferromagnetic (AF) Weyl semimetal (9, 10, 28–30). The discovery of the large spontaneous AHE is significant as it alters the pessimistic view of antiferromagnets being useless for practical applications. In fact, antiferromagnets have attracted recent tremendous attention as the next-generation active materials for spintronics, as they do not have any stray fields perturbing neighboring cells and operate at ultrafast speed (31–34). In this article, we review the recent highlights in the study of topological antiferromagnets and the associated developments in the AF spintronics, which provides the basis for developing nonvolatile memory that operates at a much faster speed and at much lower power consumption.

Another surprising property of topological magnets is the giant anomalous Nernst effect (ANE) (11, 35–37). ANE is the thermoelectric analog of AHE and generates the transverse voltage spontaneously when a magnetic conductor is exposed to a temperature gradient and, thus, heat current (instead of electric current). When the Weyl points and nodal lines are located close to the Fermi energy, the thermoelectric response due to topological fermions can be one or two orders of magnitude greater than in conventional cases (35, 38). The transverse geometry between heat current and electric voltage enables much simpler structure of a thermoelectric module in

comparison with the conventional thermoelectric converters using the Seebeck effects. In addition, we note these topological magnets can be made of only naturally abundant elements, for example, iron and manganese. These render a magnet very useful for developing energy-harvesting technology to power Internet-of-things (IoT) sensors and wearable devices (37, 39). In this era of the worldwide movement toward being carbon neutral, the development of thermoelectric magnets will become a significant new trend in the future.

Furthermore, striking properties of topological magnets are not limited to the AHE and ANE. They also provide giant optical and novel spin Hall responses at their surface and interface (33, 40–44). Here, we will review the wide range of exciting phenomena found in the bulk and interface of topological magnets that have outstanding potential for real-life applications, and thus will focus on the magnets with transition temperatures higher than room temperature.

2. TOPOLOGICAL MAGNETS

2.1. Berry Curvature in Momentum Space

Since their discovery in ferromagnets in the nineteenth century, both the AHE and ANE have been known to be proportional to magnetization. In fact, as summarized in **Figure 1**, AHE and ANE of a number of ferromagnets are found to grow roughly linearly with magnetization (30). In contrast, the topological magnets such as Mn_3Sn and Co_2MnGa show much larger AHE and ANE than those expected based on the scaling law (9, 11, 35). Such striking enhancement is caused by the Berry curvature or fictitious field arising from the nontrivial topology of the electronic structure in the momentum space (38, 45–51).

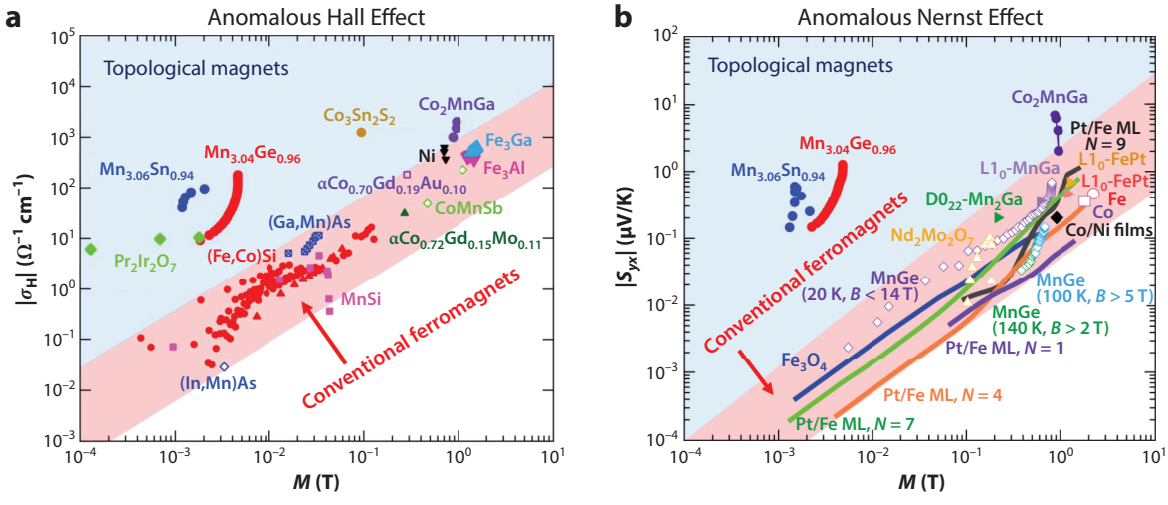

Figure 1

Topological magnets, whose transverse responses break empirical scaling law with magnetization known for conventional ferromagnets. Full logarithmic plots of (*a*) the anomalous Hall conductivity σ_H and (*b*) the anomalous Nernst signal S_{ji} versus the magnetization M for a variety of ferromagnetic (FM) metals and topological magnets measured at various temperatures and fields. As for the anomalous Hall conductivity in panel *a*, the data for the topological spin liquid $Pr_2Ir_2O_7$ are also shown. It confirms the empirical rule for ferromagnets that σ_H and S_{ji} linearly increase with M (*pink shaded region*). The Hall effect and Nernst signal data points for topological magnets obtained at various temperatures do not follow the relation and are one to three orders of magnitude higher than the scaling law. Figure adapted from Reference 30.

The intrinsic contribution to the anomalous Hall conductivity (AHC; σ_{ij}) is given by the sum of the Berry curvature ($\Omega_{n,ij}$) of the occupied bands (52, 53),

$$\sigma_{ij} = -\frac{e^2}{\hbar}\int \frac{\mathrm{d}\boldsymbol{k}}{(2\pi)^3}\sum_n f[\varepsilon_n(\boldsymbol{k}) - \mu]\Omega_{n,ij}(\boldsymbol{k}),$$

where f and ε_n are the Fermi-Dirac distribution function and energy of the nth band, respectively. The Berry curvature for the band n is given by

$$\Omega_{n,ij}(\boldsymbol{k}) = -2\mathrm{Im}\sum_{m\neq n}\frac{v_{nm,i}(\boldsymbol{k})v_{mn,j}(\boldsymbol{k})}{[\varepsilon_m(\boldsymbol{k}) - \varepsilon_n(\boldsymbol{k})]^2},$$

with

$$v_{nm,i}(\boldsymbol{k}) = \frac{1}{\hbar}\langle u_n(\boldsymbol{k})|\frac{\partial \hat{H}(\boldsymbol{k})}{\partial k_i}|u_m(\boldsymbol{k})\rangle.$$

Here, $|u_n(\boldsymbol{k})\rangle$ is the periodic part of the Bloch wave function and $\hat{H}(\boldsymbol{k}) = e^{-i\boldsymbol{kr}}\hat{H}e^{i\boldsymbol{kr}}$. The Berry curvature can be interpreted as a fictitious magnetic field and the equation of the motion of an electron is written as

$$\dot{\boldsymbol{r}} = \frac{1}{\hbar}\frac{\partial \varepsilon_n(\boldsymbol{k})}{\partial \boldsymbol{k}} - \dot{\boldsymbol{k}} \times \Omega_n(\boldsymbol{k}).$$

Note that the second term in the right-hand side of the equation deflects the motion of electrons. As shown by Karplus & Luttinger (54), even in the absence of an external magnetic field, the AHC can be finite when the time-reversal symmetry (TRS) is broken and the sum of the Berry curvature is nonvanishing.

The transverse thermoelectric conductivity α_{ij} is also represented in terms of the Berry curvature,

$$\alpha_{ij} = \frac{1}{T}\frac{e}{\hbar}\int \frac{\mathrm{d}\boldsymbol{k}}{(2\pi)^3}\sum_n \Omega_{n,ij}(\boldsymbol{k})\left\{[\varepsilon_n(\boldsymbol{k}) - \mu]f[\varepsilon_n(\boldsymbol{k}) - \mu] + k_\mathrm{B}T\ln(1 + \exp\{-\beta[\varepsilon_n(\boldsymbol{k}) - \mu]\})\right\}.$$

In the limit of low T, α_{ij} can be calculated by summing up the Berry curvature at the Fermi energy ε_F,

$$\alpha_{ij} = -\frac{\pi^2 k_\mathrm{B}^2 T}{3}\frac{e}{\hbar}\int \frac{\mathrm{d}\boldsymbol{k}}{(2\pi)^3}\sum_n \Omega_{n,ij}(\boldsymbol{k})\delta(\varepsilon_n(\boldsymbol{k}) - \varepsilon_\mathrm{F}).$$

The Berry curvature distribution in the momentum space is intimately linked with the topology in the electronic structure. In the twenty-first century, the discoveries of graphene, topological insulators, and Weyl semimetals advance our understanding of novel topological phases; yet these systems lack electronic correlation effects (1–3, 5, 6). Electronic correlation is essential for understanding magnetism, and thus the study of how the topological phases arise in magnetic conductors is highly significant. In recent years, such research becomes one of the central trends in condensed matter physics and spintronics sparked by the theoretical proposal of the magnetic Weyl semimetal phase made in 2011 (7, 8).

2.2. Magnetic Weyl Semimetals

In the field of condensed matter physics and spintronics, there has been a strong surge of interest in the Weyl fermions and their novel properties (5, 6). This relativistic fermion was first introduced in the field of high energy physics by the German Physicist, Hermann Weyl in 1929, and once thought to describe neutrinos (55). However, it remained elusive until recently being realized

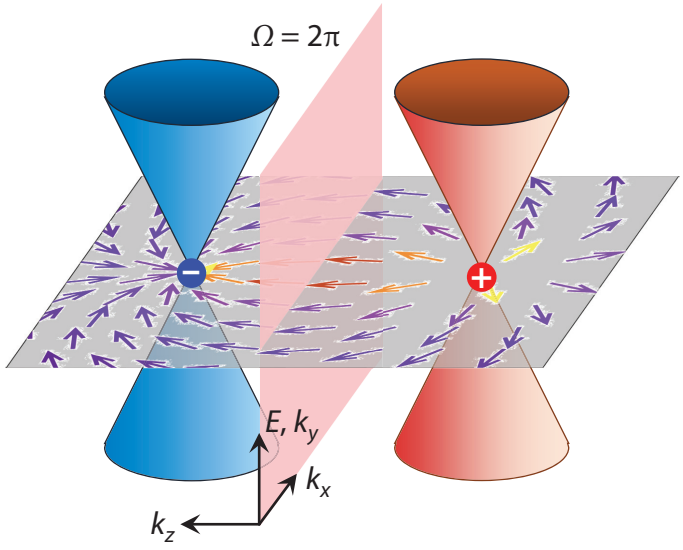

Figure 2

Schematic of the linearly dispersive (relativistic) particles, Weyl fermions. The red and blue cones indicate the linearly dispersive bands for Weyl fermions, and the crossing points (Weyl points) have either positive or negative magnetic charges that play the roles of the source or drain of the fictitious magnetic field or Berry curvature (*arrows*). The red plane normal to the direction connecting the opposite charges receives the total flux of 2π, which is a quantized value. Thus, the 2D electronic system represented by the red plane has the quantum Hall state and the 3D stacking of layers with the quantum Hall state forms the Weyl semimetal state. This is the reason why the Weyl semimetal system may exhibit large anomalous Hall and Nernst effects.

as an emergent quasiparticle in condensed matter systems, the so-called Weyl semimetal (5–7). Theoretically, Weyl fermions can be classified into two kinds: one stabilized by inversion symmetry breaking (56, 57) and the other by the TRS breaking (10–14). The latter is known as the "magnetic Weyl fermions." Historically, the Weyl fermions were first identified in an inversion breaking state of weakly interacting electron systems (56, 57). Subsequently, the worldwide search turns its focus to Weyl quasiparticles in a magnetically ordered state that spontaneously breaks TRS, leading to the discovery of Weyl fermions in a correlated metal (10–14).

As a heuristic argument, let us consider the simplest case of a Weyl semimetal that hosts a pair of linearly dispersive bands forming cone type structure near the Fermi energy (**Figure 2**). Here, we consider a system with an inversion symmetry but without TRS so that two Weyl points in a pair has the same energy.

Each band crossing is described by a 2×2 Hamiltonian,

$$H(\boldsymbol{k}) = f_0(\boldsymbol{k})\mathbf{1} + f_1(\boldsymbol{k})\sigma_x + f_2(\boldsymbol{k})\sigma_y + f_3(\boldsymbol{k})\sigma_z,$$

where $\mathbf{1}$ is the unit matrix and $\sigma_i (i = 1, 2, 3)$ are the Pauli matrices, respectively. If $f_1(\boldsymbol{k}_0) = f_2(\boldsymbol{k}_0) = f_3(\boldsymbol{k}_0) = 0$, the band touching occurs at $\boldsymbol{k} = \boldsymbol{k}_0$. We can then expand H around $\boldsymbol{k} = \boldsymbol{k}_0$ as

$$H(\boldsymbol{k} = \boldsymbol{k}_0 + \Delta\boldsymbol{k}) = f_0(\boldsymbol{k}_0)\mathbf{1} + (\boldsymbol{v}_0 \cdot \Delta\boldsymbol{k})\mathbf{1} + \sum_{i=1,2,3} (\boldsymbol{v}_i \cdot \Delta\boldsymbol{k})\sigma_i,$$

where $\boldsymbol{v}_\mu = \nabla f_\mu(\boldsymbol{k} = \boldsymbol{k}_0)$ ($\mu = 0,1,2,3$). This is essentially the same as the Weyl Hamiltonian for the massless Dirac equation with a positive and negative chiral charge

$$H = \pm \boldsymbol{p} \cdot \boldsymbol{\sigma},$$

where $\boldsymbol{p} = i\boldsymbol{\partial}$.

Because the Weyl Hamiltonian contains all the Pauli matrices, σ_x, σ_y, and σ_z, symmetry breaking perturbation such as magnetic impurity and thermal fluctuations cannot easily gap out the Weyl nodes. Thus, the Weyl semimetal state is beautifully robust against perturbations, a crucial property for applications.

The stability of the Weyl semimetal state is rooted in the topological character of the crossing point, which cannot be gapped out unless two of opposite chirality meet. The Weyl nodes are source and drain of the Berry curvature and can be viewed as magnetic monopoles, leading to various interesting phenomena, such as layered quantum Hall effect (45, 58), and chiral anomaly (59, 60). The distribution of Berry curvature in the momentum space is uniquely determined by the distribution of magnetic monopoles in the momentum space, following the Gauss's law of electromagnetism. In fact, by using this analogy one can easily understand how the quantum Hall effect arises in the Weyl semimetal (**Figure 2**).

2.3. Layered Quantum Hall Effect

Here we consider a special case where the Weyl points are located exactly at the Fermi energy. Then, the Fermi surface of the semimetal is only two points and the rest in the momentum space is gapped semiconducting states. Now the direction connecting the two Weyl points is along the TRS breaking axis determined by the magnetic ordering such as magnetization direction and polarization axis of multipole order, which we will discuss in Section 2.5. If we take this TRS breaking axis along the z-axis, the two-dimensional (2D) electronic plane on the xy plane becomes special if it is located in the middle of the line connecting the two Weyl nodes (**Figure 2**). Namely, the Berry curvature determined by the size of the magnetic monopoles penetrates through the plane along the z axis, i.e., along the normal direction of the 2D electronic plane. As the magnetic charge is quantized, the total Berry flux passing through the plane is also quantized to be 2π. The 2D electronic system with the total Berry flux of 2π penetrating along the normal direction is exactly what is necessary to realize the quantum Hall effect. Thus, the Weyl semimetal may exhibit the layered quantum Hall effect spontaneously at zero field. In fact, this spontaneous Hall effect is the simplest case of the AHE driven by the intrinsic mechanism. By further extending this argument, one may conclude that the intrinsic mechanism of the AHE is based on the Berry curvature in the momentum space (52, 53).

Generally, internal field comes from the spin polarization due to magnetic moment of magnetic ions. In contrast, the fictitious field originates from the Berry phase of the electronic wave function. Thus, the above mechanism of AHE in the Weyl semimetal clearly indicates that the AHE is not necessarily proportional to the size of the magnetic moment or magnetization and could be in principle independent from magnetization. Experimentally, such a case has been found in a spin liquid state in a spin ice compound $Pr_2Ir_2O_7$ prior to the theoretical proposal of Weyl semimetal (4, 61, 62). This discovery has further motivated the search of a large AHE in antiferromagnets with vanishingly small magnetization. The first experimental realization was made in the noncollinear antiferromagnet Mn_3Sn (9). The system exhibits the AHE that is as large as those in ferromagnets despite that they exhibit no or a very tiny amount of the magnetization, one thousandth of the FM counterpart (**Figure 1**). The discovery breaks the empirical law that had never been challenged for more than a century.

2.4. Anomalous Nernst Effect and Magnetic Weyl Fermions

A Weyl semimetal possesses the Weyl points nearby the Fermi energy E_F and thus various effects of Weyl fermions can be observed in the transport properties. One of the prominent effects is the ANE, which is the thermoelectric counterpart of the AHE.

As in the Hall effect measurements, the anomalous Nernst signal S_{ij} can be measured by employing the same electrodes by applying a heat flow instead of a charge current. Perpendicular to both the magnetic field B and the heat current $Q_i = -\nabla_i T$, a transverse voltage V_j is induced through the ANE. The anomalous Nernst coefficient is estimated as $S_{yx} = E_y/\nabla_x T$ and is composed of two components due to (*a*) the transverse charge flow coming from the transverse thermoelectric current $\alpha_{yx}(-\nabla_x T)$ and (*b*) the Hall current, i.e., $S_{yx} = \alpha_{yx}\rho_{xx} - \sigma_{yx}\rho_{xx}S_{xx}$ (63, 64). Here, E_y, ρ_{xx}, σ_{yx}, and S_{xx} are the transverse electric field, longitudinal resistivity, Hall conductivity, and Seebeck coefficient, respectively.

In topological magnets, the first term is normally dominant, as α_{yx} is proportional to the Berry curvature at the Fermi energy, as discussed in Section 2.1 (53, 65). Therefore, ANE could be potentially large in a magnetic Weyl semimetal as the Weyl fermions may induce a large Berry curvature at E_F. Empirically, the ANE is known to be proportional to the size of magnetization similarly to AHE, and thus has been seen only in ferromagnets, since its early study by Smith in 1911 (66). Breaking this empirical rule, recent studies on the AF Weyl semimetal Mn_3Sn has found that the system may exhibit an ANE as large as those found in ferromagnets despite the fact that it only carries vanishingly small magnetization (**Figure 1**; 35, 67). Further discussion of the striking properties will be made in Section 3.1.

The discovery has motivated further study on the mechanism to enhance the density of states (DOS) of Weyl fermions so that the Berry curvature near the Fermi energy can be strongly enhanced. One approach is to locate a material close to the quantum Lifshitz transition between type-I and type-II Weyl semimetals (11). The type-I Weyl semimetals are characterized by either the electron or hole type of Weyl fermions, depending on the location of the chemical potential. The typical one is shown in **Figure 3**. By contrast, the type-II Weyl semimetals possess both electron and hole types of Weyl fermions owing to the tilting of the Weyl cones (68) (**Figure 3*c***). With continuous tilting of the Weyl cones, a quantum Lifshitz transition takes place and separates the type-I and type-II Weyl semimetal states. Exactly at the Lifshitz quantum critical point, a flat band emerges with an enhanced DOS of the band with Weyl points and, thus, with enhanced Berry curvature (**Figure 3*a***). An analytical calculation indicates that this transition leads to a logarithmic divergence of the transverse thermoelectric conductivity and may lead to a large ANE (**Figure 3*f***). In fact, this has been first discovered in the FM Weyl semimetal Co_2MnGa (**Figure 3*d***). Notably, this material exhibits an ANE reaching $\sim 8\,\mu$V/K, which is one order of magnitude greater than previously reported values (**Figure 3*e***; 11, 69, 70). Furthermore, recent angle-resolved photoemission spectroscopy (ARPES) measurements have confirmed the electronic structure associated with the Weyl points near the Fermi energy and its proximity to the quantum Lifshitz transition point (13, 71).

Among various relativistic particles in condensed matter systems, magnetic Weyl fermions are particularly significant as they exist robustly in three dimensions even with symmetry breaking fields as well as with thermal fluctuations at high temperatures. Furthermore, they exhibit a variety of exotic phenomena, such as large spontaneous Hall and Nernst effects, and emergent electromagnetism (**Figure 1**). In addition, unlike the other nonmagnetic version of Weyl fermions, one may control the location of the Weyl points in momentum space by a magnetic field and other equivalent means, such as spin current injections, as we discuss in Section 3.7. At the same time, the fact that one may easily control the magnetic Weyl fermions at room temperature indicates

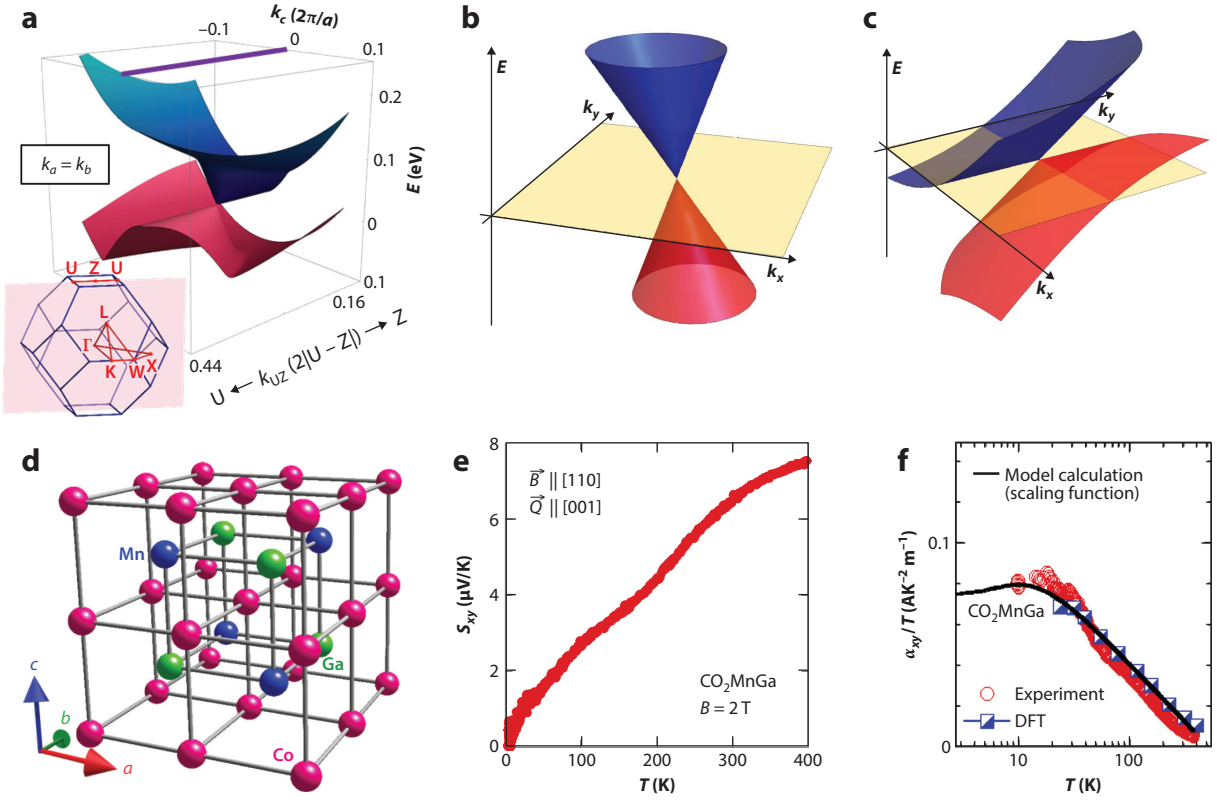

Figure 3

Quantum Lifshitz transition of a Weyl semimetal state and logarithmic divergence in the anomalous Nernst effect. (*a*,*b*,*c*) Dispersion relation around the Weyl point near the quantum Lifshitz transition in (*a*) the full Heusler ferromagnet Co_2MnGa and in (*b*) type-I and (*c*) type-II Weyl semimetals. (*d*) Crystal structure of Co_2MnGa. (*e*,*f*) Temperature dependence of (*e*) the Nernst coefficient and of (*f*) the transverse thermoelectric coefficient divided by temperature α_{xy}/T of the FM Weyl semimetal Co_2MnGa. Experimental results of α_{xy}/T (*red circles*) agree well with analytical (*solid line*) and computational (*square*) calculations and show a ln *T* dependence. Figure adapted from Reference 11.

that such a Weyl magnet will be useful for fundamental research of spintronics and energy harvesting technology. In Section 3.1 below, we take the AF Weyl semimetals as a prime example and show their striking properties essential for developing AF spintronics. Before doing so, we introduce the concept of a magnetic cluster multipole (CMP) in the following section. This is essential for understanding the topological antiferromagnets as it plays a role of a real space handle to control the magnetic Weyl fermions in momentum space, similar to magnetization in the case of the ferromagnets.

2.5. Cluster Magnetic Multipole Theory

As we have seen in the previous sections, the Weyl nodes are the source and drains of Berry curvature, and thus Berry curvature diverges at the nodes. However, the existence of Weyl points alone does not guarantee the finite size of AHE or ANE. Instead, the sum of the Berry curvature in momentum space must be finite, and thus the distribution of magnetic charges at the nodes must break the TRS. Whereas in a ferromagnet it is clear that its magnetization breaks the TRS

and controls the size of the responses, no such measure was available for antiferromagnets. Thus, it would be very useful if one could introduce a real-space quantity equivalent to magnetization that characterizes the anomalous transverse transport in magnetic materials in general.

When we consider constructing such a quantity, it is critically important to take account of the symmetry of the local spin configuration of a magnet. Indeed, Kleiner has shown that the structure of the transport coefficients is exactly determined by the magnetic point group symmetry of the system (72–75). For this problem, we can utilize the idea in a textbook of quantum chemistry, where we classify the electronic states in the Coulomb potential into the *s*, *p*, *d*, and *f* orbitals using the spherical harmonics. Similarly, when the energy scale of the spin-orbit coupling is larger than that of the crystal field splitting, the complex magnetic distribution around a nucleus can be represented using magnetic multipoles,

$$M_{\ell m} = \sqrt{\frac{4\pi}{2\ell+1}} \sum_j \left(\frac{2\boldsymbol{\ell}_j}{\ell+1} + \boldsymbol{\sigma}_j \right) \cdot \boldsymbol{O}_{\ell m}(\boldsymbol{r}_j),$$

with

$$\boldsymbol{O}_{\ell m}(\boldsymbol{r}) \equiv \nabla \left[r^\ell Y^*_{\ell m}(\hat{\boldsymbol{r}}) \right].$$

Here, $\boldsymbol{\ell}_j$ and $\boldsymbol{\sigma}_j$ are the orbital and spin angular momentum of the *j*th electron at $\boldsymbol{r}_j$, respectively, and $Y_{\ell m}$ is the spherical harmonics with $\hat{\boldsymbol{r}} = \boldsymbol{r}/r$ and $r = |\boldsymbol{r}|$. The magnetic multipoles at atomic sites are known to exhibit various intriguing phenomena in strongly correlated electron systems and *f*-electron systems (76–78).

We can generalize this idea to characterize a complex spin configuration in antiferromagnets. Namely, we can define multipole moments for a cluster of atoms, i.e., CMP moments (79, 80),

$$M_{\ell m} \equiv \sqrt{\frac{4\pi}{2\ell+1}} \sum_{i=1}^{N_{\text{atom}}} \boldsymbol{m}_i \cdot \boldsymbol{O}_{\ell m}(\boldsymbol{R}_i),$$

where N_{atom}, $\boldsymbol{m}_i$, and $\boldsymbol{R}_i$ are the number of magnetic atoms in the cluster, local magnetic moment of the *i*th atom, and position of the *i*th atom, respectively. By using CMP, we can classify any spin configuration in the common framework. Ferromagnets have a ferroic order of cluster dipole, and antiferromagnets have a ferroic order of high-rank multipoles.

Recently, it has been shown that Mn_3Sn and Mn_3Ge have a ferroic order of a magnetic cluster octupole (79) (**Figure 4*b***, *inset*), whose irreducible representation is the same as that of a magnetic dipole. Therefore, we can interpret that the anomalous transverse transport in Mn_3Sn and Mn_3Ge is induced by octupolarization. This can be clearly seen when we plot the AHC as a function of the polarization of the magnetic CMP. In **Figure 4**, we show the AHC of the FM state in elemental Fe as a function of the magnetization (*M*). When *M* is small, the AHC is proportional to *M*. With increasing *M*, the AHC increases, and eventually it decreases after forming a peak. This dome-like behavior of the AHC is commonly seen in many ferromagnets (52). Plotting the AHC of Mn_3Sn and Mn_3Ge as a function of the octupolarization, we see that it also has the dome-like structure. This result indicates that CMP quantitatively characterizes the anomalous transverse transport in both ferromagnets and antiferromagnets. More recently, it has also been shown that CMP is a powerful tool for spin-dynamics simulation (81) and magnetic structure prediction (82).

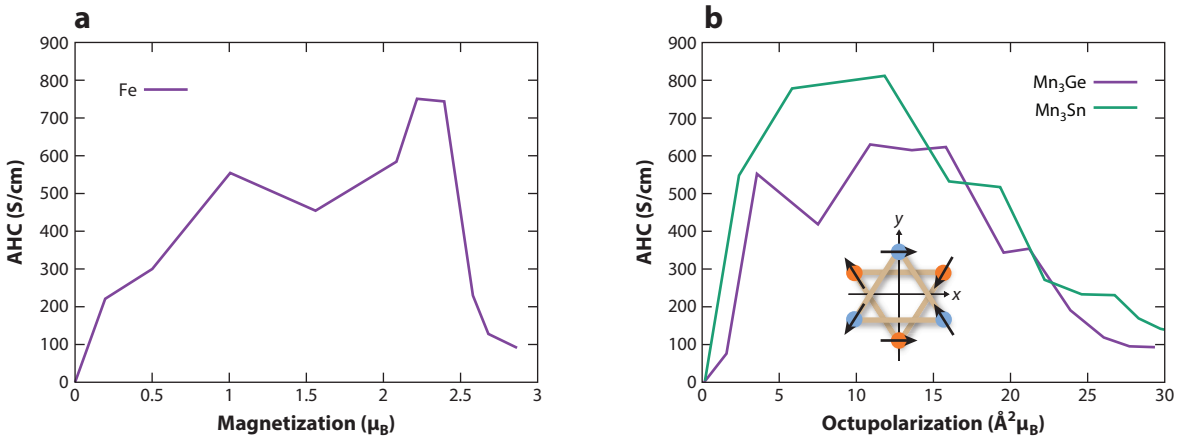

Figure 4

AHC of Fe and Mn_3X (X = Sn, Ge). Although the AHC of Fe is plotted as a function of magnetization (in panel *a*), that of Mn_3X is plotted as a function of octupolarization (in panel *b*). We see that the AHC commonly shows a dome-like structure, indicating that the CMP is a convenient quantity to characterize the anomalous transverse transport in both ferromagnets and antiferromagnets. Inset indicates the cluster octupole consisting of six magnetic moments of Mn. The octupole polarization is along the *x* axis. Abbreviations: AHC, anomalous Hall conductivity; CMP, cluster multipole.

3. TOPOLOGICAL ANTIFERROMAGNETIC SPINTRONICS

3.1. Antiferromagnetic Spintronics

Since the discovery of magnetism around 500 BC, ferromagnetism has been the only magnetic state of matter utilized for application. For a long time, it has been employed mainly for a compass for navigation. Much later in the nineteenth century, based on the formulation of electromagnetism, the ferromagnet has enabled various functions such as motors, generators, and power transformation. In the late twentieth and early twenty-first centuries, the experimental discovery of giant magnetoresistance, tunneling magnetoresistance, the spin–transfer torque, and spin–orbit torque (SOT) has placed ferromagnets as the main active materials for memory devices (83).

Another form of magnets that is far more naturally abundant than ferromagnets is antiferromagnets. In contrast with ferromagnets, the existence of antiferromagnets had not been confirmed until the middle of the twentieth century when the neutron diffraction method became available (84). Although a number of basic research studies have revealed their fascinating properties to date, antiferromagnets have been considered much less useful for applications; AF materials also have magnetically ordered states, where their spins are normally aligned antiparallel with their neighbors, resulting in no overall magnetization. Such spin states are notoriously difficult to control, making writing, reading, and storing magnetic data seemingly impossible.

Meanwhile, recent rapid growth in information technology has demanded the spintronic device to acquire a higher integration density and higher speeds for processing data, for example, in the nonvolatile magnetic memory device. For this, antiferromagnets have actually attracted recent attention as an active material for next-generation memory devices (31–34, 85, 86); unlike the ferromagnets that are typically used for spintronics, antiferromagnets are not easily disturbed by external magnetic fields and, more importantly, they produce almost no stray fields of their own. As FM memory devices reach limits of miniaturization, the use of antiferromagnets would allow for even higher storage density. In addition, without stray fields, antiferromagnets are free from shape anisotropy (87), which is in sharp contrast with ferromagnets. Furthermore, antiferromagnets have

much faster spin dynamics than ferromagnets, opening new avenues for ultrafast data processing. In fact, the first demonstration of the electric current manipulation of spin order was made in an antiferromagnet in 2016 (88). Still, in order to employ antiferromagnetism, a number of obstacles exist. For example, there is no established way of reading information except relying on a very weak effect called anisotropic magnetoresistance (AMR; 88, 89).

In this section, we discuss the recent discovery of a new type of functional antiferromagnets, the first example of a topological Weyl magnet, that exhibits a variety of new functions that have never before been seen in AF metals (9, 10, 28–30, 35, 40, 41, 43). After introducing the discovery of (*a*) the AHE in an antiferromagnet (9, 28, 29), we review (*b*) the evidence for magnetic Weyl fermions (10). Then, we discuss the following new phenomena in an AF metal, namely, (*c*) the ANE (35), (*d*) magnetic optical effects (40, 42), (*e*) the magnetic spin Hall effect (MSHE) (41), and (*f*) electric switching of AF domains (43, 90).

3.2. Observation of a Large Anomalous Hall Effect in an Antiferromagnet

For detecting the magnetic state in ferromagnets, one well-known means is the AHE, which arises in ferromagnets even in the absence of an external field (**Figures 1*a*** and **5*a***; 91). Since its discovery by Edwin Hall in 1880 (92), the AHE is known to be proportional to magnetization and, thus, only observed in ferromagnets (91). However, as we discussed in Section 2.2, recent understanding of the AHE based on the Berry phase concept (52) has suggested that it could arise even in magnets with zero magnetization, including antiferromagnets (46, 93, 94). The first observation of a spontaneous Hall effect in a magnetic state without magnetization was made in a spin liquid state of the metallic spin ice $Pr_2Ir_2O_7$ in 2009 (4, 61, 62). Strikingly, despite the fact that the spin liquid exhibits the zero or vanishingly small magnetization, the AHC is found to emerge spontaneously and exceeds 10 $\Omega^{-1}cm^{-1}$. This has motivated further searches for AHE in antiferromagnets, which in principle are far more naturally abundant than spin liquids.

Five years later, the first example of the AHE in an antiferromagnet was discovered experimentally (9). Experiments were made in particular for the AF metal Mn_3Sn and initiated independently prior to the theoretical proposal made on the AHE in the material (47). Strikingly, the effect is found to be unusually large, exceeding 100 $\Omega^{-1}cm^{-1}$, which is even larger than values seen in ordinary ferromagnets (52, 91). Mn_3Sn has a hexagonal lattice supporting an inverse triangular spin structure (95, 98; **Figure 5*b***). It is one of the Kagome metals that has attracted significant attention (9, 12, 25–27, 99) and harbors one type of the chiral magnetic structures, which are known to provide a variety of interesting phenomena (17). It exhibits AHE at room temperature, and furthermore it can be switched by a weak magnetic field (9). This discovery indicates that the AHE arises not from the internal magnetic field as in ferromagnets but from the large fictitious field or Berry curvature (equivalent to the effect due to an external field of a few 100 T), which is driven by nontrivial topology of the electronic band structure of the material (**Figure 5*b***), which is discussed in terms of the Weyl fermions in Section 3.3 (10). Furthermore, the observation indicates that even though the magnetization is ~1,000 times smaller than in an ordinary ferromagnet, a tiny magnetic field of about a few 100 Oersted is enough to switch the direction of the spin state in the antiferromagnet (**Figure 6*i***) and, hence, to change the orientation of the large fictitious field.

3.3. Evidence for Weyl Fermions

Significantly, it is in the antiferromagnet Mn_3Sn where the magnetic Weyl fermion state was first found experimentally among many other correlated metals (10). After the AHE was experimentally

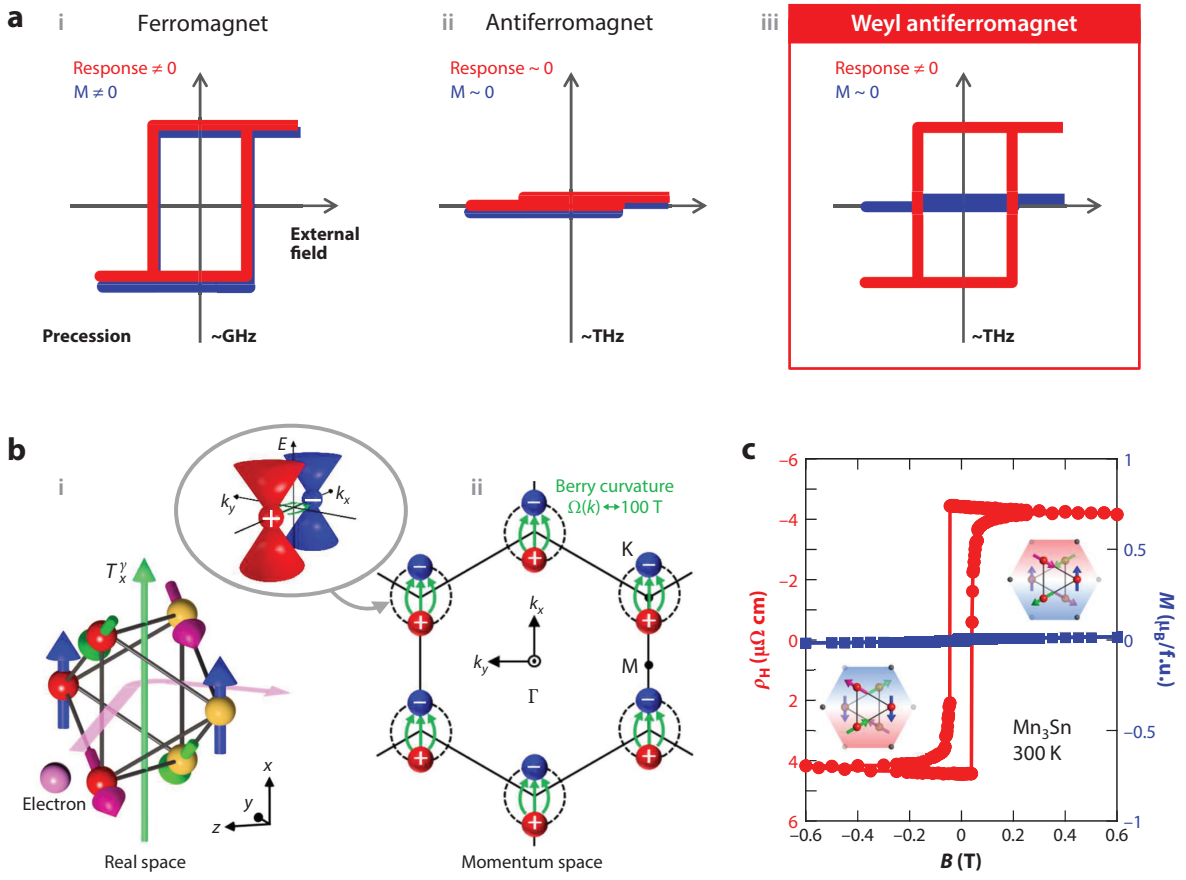

Figure 5

Large responses due to the combination of magnetic octupole and Weyl fermions in a Weyl antiferromagnet and Mn_3Sn. (*a*) Macroscopic responses such as anomalous Hall and Nernst effects are large in ferromagnets and scale with magnetization (*a*, *i*). Such effects are not known for ordinary antiferromagnets because of their negligibly small magnetization (*a*, *ii*). However, in Weyl antiferromagnets or antiferromagnetic Weyl semimetals (*a*, *iii*), macroscopic responses can be very large despite vanishingly small magnetization and are driven by the fictitious field (equivalent to 100 to 1,000 T) induced by the nontrivial topology of electronic band structure such as Weyl points in momentum space. Furthermore, such a giant response can be switched not only by magnetic field but by electrical current. (*b*, *i*) Real space crystal and spin structure of Mn_3Sn, highlighting a magnetic octupole T_x^y. Each Mn has a magnetic moment (*arrow*). An inverse triangular spin structure appears because of the geometrical frustration resulting from the Kagome lattice formed by Mn (see 27, 30, 95–97). (*b*, *ii*) Momentum space distribution of the Weyl points with different magnetic charges (chiralities) on the $k_z = 0$ plane in Mn_3Sn when M is aligned along the x direction. The inset depicts the linearly dispersive modes around a pair of Weyl points with different charges. (*c*) Magnetic field dependence on the Hall resistivity (*left*) and magnetization (*right*) in Mn_3Sn at room temperature. Figure adapted from Reference 9.

discovered, Mn_3Sn was proposed to be a magnetic version of Weyl semimetal based on the band structure calculations (**Figure 5*b***; 48). The chiral spin structure of Mn_3Sn and Mn_3Ge (**Figure 5*b***) lowers the original hexagonal crystal symmetry to orthorhombic. **Figure 5*b*** schematically shows the theoretically predicted distribution of the Weyl points in the $k_z = 0$ plane for Mn_3Sn (10, 48). The mirror symmetries ensure that the Weyl points appear along a $\boldsymbol{k}$ direction parallel to the orientation of the magnetization $\boldsymbol{M}$. For instance, when $\boldsymbol{M} \parallel x$, the Weyl points locate along the Brillouin zone boundary connecting high symmetry points K-M-K (**Figure 5*b***).

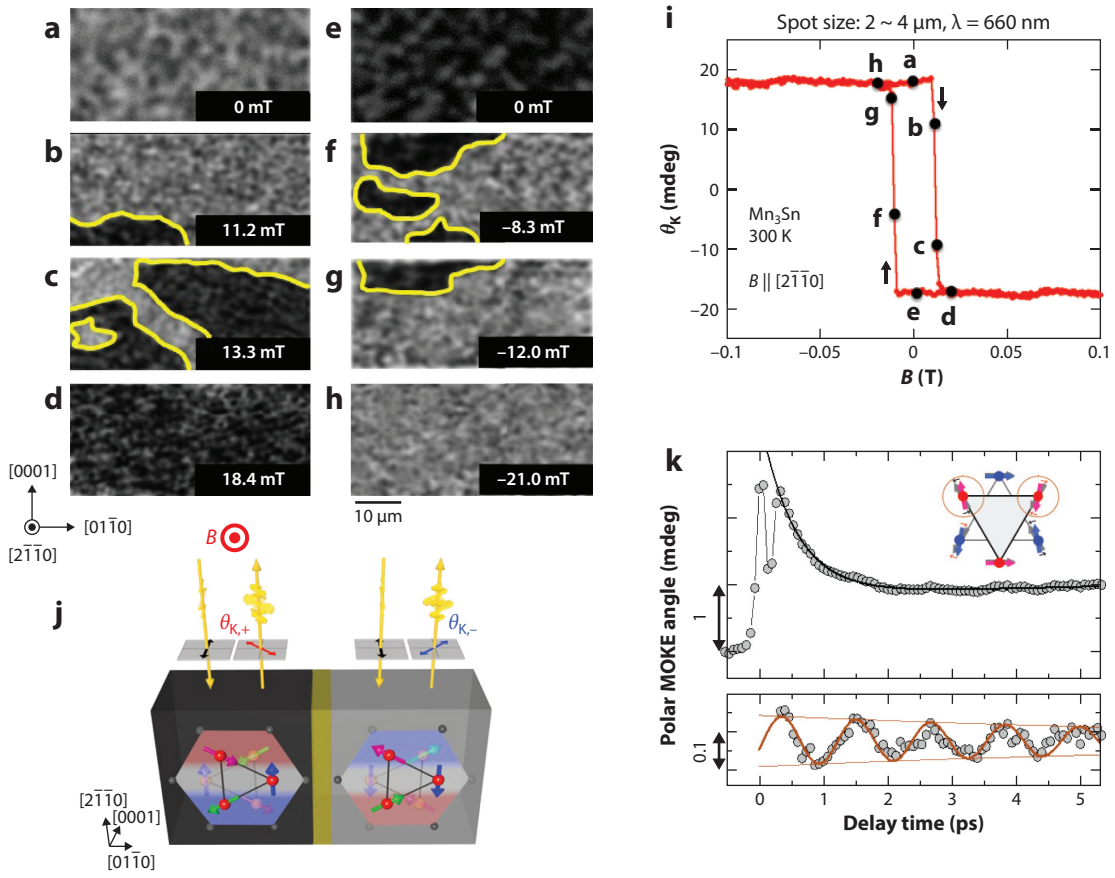

Figure 6

Visualization of magnetic octupole domains and ultrafast damped precession by the MOKE in the antiferromagnetic Weyl semimetal Mn_3Sn. Evolution of the antiferromagnetic domains as a function of a field. Gray and black regions correspond to positive and negative values, respectively, of the MOKE signal. (*a–h*) MOKE images obtained in the increasing (*a–d*) and decreasing (*e–h*) field processes. (*i*) Magnetic field dependence of the magneto-optical Kerr angle at room temperature. (*j*) Schematic illustration of two regions with different MOKE image contrasts (*gray* and *black areas*) due to opposite signs of the Kerr angles, $\theta_{K+/-}$, corresponding to two types of cluster magnetic octupole domains that have the inverse triangular spin structures with opposite spin directions within the (0001) plane. The two regions are separated by a domain wall (*yellow area*), which may be chiral and topological in character (see 111, 112). (*k*) Time-resolved MOKE signal taken under a field of 2 T along the *a* axis of Mn_3Sn. The background signal (*solid curve*) is subtracted from the data in the upper panel and the rest are plotted in the lower panel. A clear oscillation with a frequency of ~0.9 THz is seen due to the ultrafast damped precession of the magnetic octupole, as illustrated in the inset of the upper panel (110). Panels *a–j* adapted with permission from Reference 40. Panel *k* adapted from Reference 110. Abbreviation: MOKE, magneto-optical Kerr effect.

Clear evidence for strong electron correlation in Mn_3X (X = Sn, Ge) compounds is the large renormalization factor of ~5 found in ARPES measurements. Such dramatic bandwidth renormalization is comparable with that typically observed in copper and iron-based high-temperature superconductors as well as 4*f*-electron-based heavy fermion compounds, therefore posing an intrinsic challenge for direct observation of Weyl fermions. Nevertheless, to examine the theoretical predictions, extensive ARPES measurements on Mn_3Sn have been made (10) and the key signatures of Weyl fermions found, including (*a*) the photon intensity map showing remarkable agreement with the predicted electron-type Fermi pocket hosting Weyl fermions; (*b*) energy

dispersions of the ARPES intensity map, which were all found to be consistent with the theoretical band dispersion after renormalizing the energy scale; and (*c*) the momentum distribution curve providing strong evidence for the band-crossing between the electron and hole bands producing Weyl nodes near E_F along K-M-K.

The gapless nature of the Weyl fermions renders their acute responses in low-energy probes, with the magneto-transport phenomena known as the chiral anomaly (59, 60). In the presence of a high magnetic field, the linear crossing points are quantized into Landau levels, resting chiral lowest Landau levels for each Weyl crossing. Consequently, electrons occupying the lowest Landau levels are divided into left- and right-moving groups of opposite chirality. In a hypothetical case in which these two groups do not hybridize, a separate number conservation law holds for the three-dimensional left- and right-handed Weyl fermions. When an electric field and magnetic field are applied parallel to each other, the conservation law is no longer valid owing to the mixing of the left- and right-handed fermions (59, 60). This phenomenon is known as the chiral anomaly. When $E \parallel B$, the charge pumping between the Weyl nodes of opposite chirality generates the positive longitudinal magnetoconductivity (LMC) or the negative longitudinal magnetoresistivity (LMR). Meanwhile, the perpendicular configuration $E \perp B$ suppresses the chiral anomaly and leads to a negative LMC or a positive LMR owing to the normal scattering mechanism (100). Thus, the observation of the positive LMC for $E \parallel B$ and the negative LMC for $E \perp B$ provides the evidence for Weyl fermions and has been widely used in the studies of both nonmagnetic and magnetic Weyl semimetal candidates (10, 11, 57, 79, 101–104).

In fact, a clear anisotropic transport signature is obtained for Mn_3Sn at 60 K. When the magnetic field *B* is applied parallel to the electric field *E*, a positive magnetoconductance is observed, whereas the negative magnetoconductance appears in the $E \perp B$ configuration. This anisotropic magnetoconductivity is found evident also in the field angle dependent measurements. In sharp contrast with LMC due to spin fluctuations, the magnitude of the observed positive LMC for $E \parallel B$ rises and the anisotropy of the LMC becomes more pronounced in Mn_3Sn on cooling from 300 K down to 60 K. The observed large, strongly anisotropic LMC in a magnet is unprecedented, providing strong evidence for the chiral anomaly originating from the Weyl fermions (30). In addition, the temperature dependence of the thermal Hall conductivity and its comparison with AHC confirms the intrinsic Berry curvature mechanism of the transverse transport and the dominant contribution from Weyl fermions (30, 67, 105–107). Further details on the evidence for Weyl fermions can be found in Reference 30.

3.4. Large Anomalous Nernst Effect and Berry Curvature Due to Weyl Fermions

Recently, the first observation of a large ANE in an antiferromagnet has been reported (35, 67). Strikingly, the ANE in Mn_3Sn is found to be more than 100 times larger than the estimate derived from its magnetization, on par with the highest value measured for an FM metal (**Figure 1*b***; 35, 67). The large Nernst effect has been also found in Mn_3Ge (30, 108).

Generally, ANE can be described by two components, one coming from the intrinsic transverse voltage induced by the heat flow and the other originating from the AHE generated by the Seebeck effect. Hypothetically, the intrinsic component provides the direct measure of the Berry curvature at the Fermi energy (53). In Mn_3Sn, experiment finds that the dominant part of the Nernst effect comes from the intrinsic component and indicates the extremely enhanced Berry curvature near the Fermi energy in the system. Thus, the source of the Berry curvature must be near the Fermi energy and in this case the Weyl points, as discussed in Section 3.3. Furthermore, experiments on two crystals with different compositions were quantitatively consistent with calculations performed by first-principles calculations, again confirming the effect of Berry

curvature due to the Weyl fermions as the source of the large fictitious magnetic field (30). The ANE was found useful for imaging the magnetic domains by taking advantage of a laser-induced local thermal gradient (109).

3.5. Visualization of Magnetic Octupole Domains and Ultrafast Damped Precession by the Magneto-Optical Kerr Effect

The magneto-optical Faraday and Kerr effects have been widely used for various applications including magneto-optical recording technology as well as a powerful tool to probe the electronic and magnetic properties of magnetic materials (113–115). However, its observation has been restricted mostly to ferro- and ferrimagnets since their discovery in the late nineteenth century. This is because the Kerr effect was empirically known to be proportional to magnetization and believed to be absent in magnets with a vanishingly small magnetization.

Following the discovery of AHE in an antiferromagnet, another first observation of a large Kerr effect in an AF metal has been made in the noncollinear antiferromagnet Mn_3Sn (40). Theoretically, the magneto-optical Kerr effect (MOKE) can be considered as a dynamical version of the AHC and was predicted for the noncollinear antiferromagnet Mn_3Ir (116). The observed Kerr rotation angle for Mn_3Sn is exceptionally large at ∼20 millidegrees (**Figure 6*i***) and has the same size as those found in ferromagnets; in addition, it is available at room temperature, thus allowing us to use it for real-time imaging of magnetic domains and domain walls (111, 112). The MOKE microscopy has visualized for the first time the reversal of AF domains in a metal (**Figure 6*a–b***). This clearly indicates that the observed Kerr effect may well be useful not only for the study of the dynamics of AF domains but also to read the information magnetically stored in the antiferromagnet. A large MOKE signal has also been observed in the chiral antiferromagnet Mn_3Ge (117). It has been also pointed out that the X-ray magnetic circular dichroism (XMCD), which is normally not observed for an AF state, may be useful to visualize the magnetic octupole domains even though they do not carry any magnetization (118, 119). Further details on the observation and manipulation of the octupole domain using MOKE and other methods can be found in Reference 44.

Recent successful fabrication of the high-quality thin films (120–126) has allowed the measurements of transmission THz spectroscopy and, thus, the first observation of the Faraday effect at room temperature in an antiferromagnet (42). The corresponding AHE at terahertz frequencies is large, ∼20 $\Omega^{-1}cm^{-1}$, which is nearly the same value at the direct current (DC) limit and demonstrates the picosecond readout for the AF spintronics using Mn_3Sn. This was followed by the first observation of the time-resolved MOKE in the Weyl antiferromagnet Mn_3Sn by Miwa et al. (110), who have confirmed that the AF switching can be as fast as several picosecond periods due to the exchange-enhanced ultrafast damped precession (see also 81; **Figure 6*k***).

3.6. Magnetic Spin Hall Effect

The magnetic moment couples to magnetic field via dipolar interaction, and this indirect coupling has long been used to control magnetization. As an exciting recent development, direct coupling between spin polarization and charge current through the spin Hall effect (SHE) has been established (128–135). In the SHE, the spin-orbit interaction plays an essential role. Importantly, the effect enables us to manipulate the magnetic moment via spin–transfer torque in a smaller length scale. The spin Hall technique also has the potential for low-energy magnetic storage devices. Because of this practical motivation, and also because of fundamental interest in fully understanding the effect, spin Hall properties of many kinds of materials have been intensively investigated.

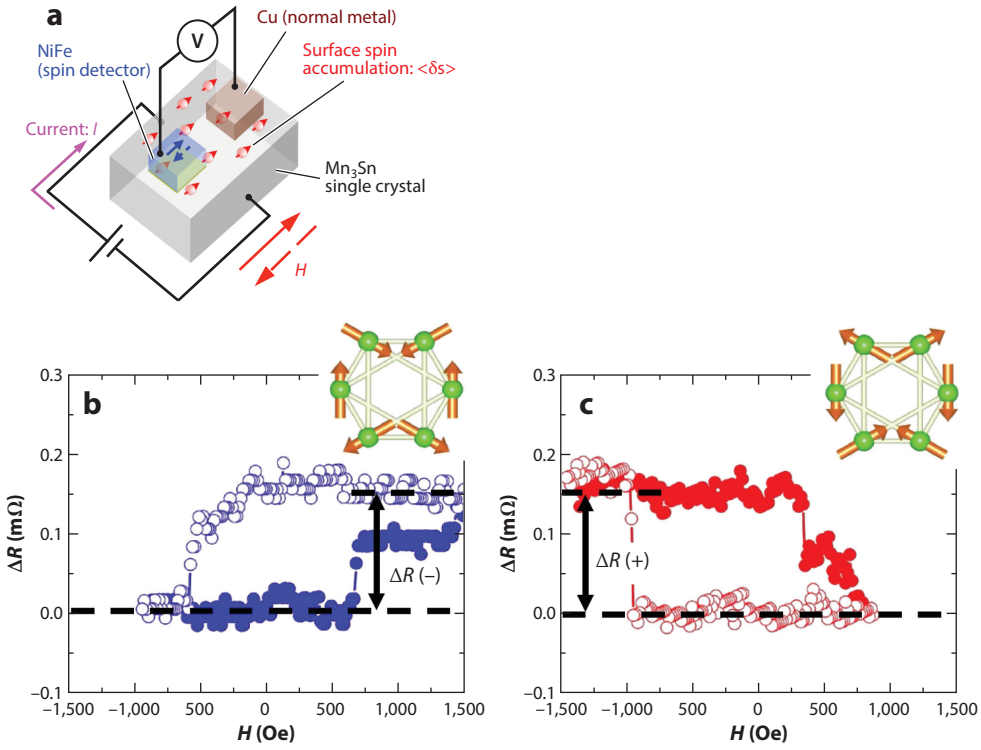

Figure 7

Magnetic SHE discovered in the antiferromagnetic Weyl semimetal Mn_3Sn. (*a*) Measurement configuration to detect the surface spin accumulation δs induced by current I. Two electrodes, respectively made of ferromagnetic NiFe and nonmagnetic Cu, are attached on a microfabricated single crystal of Mn_3Sn. (*b*,*c*) Magnetic field H dependence of the resistance change ΔR due to the spin accumulation formed at the surface of the antiferromagnetic Weyl semimetal Mn_3Sn at room temperature. The shift of electrochemical potential across the interface between Mn_3Sn and NiFe detects the spin accumulation induced by the current passing through Mn_3Sn and generates the voltage V between NiFe and Cu electrodes. The rectangular hystereses (*b*,*c*) observed upon the magnetization reversal of NiFe indicate the existence of the spin accumulation due to the SHE of Mn_3Sn. By applying a large field rather than a switching field (around 0.5 T) of Mn_3Sn, the cluster octupole in Mn_3Sn can be switched (*insets* in panels *b* and *c*). Strikingly, the polarity of the hysteresis curve, and thus the direction of accumulated spins, changes corresponding to the reversal of the octupole polarization in Mn_3Sn (*b*,*c*). This demonstrates that the dominant contribution to the SHE in Mn_3Sn is odd under TR, which is in sharp contrast with the ordinary SHE, which is even under TR (see 41, 127). Figure adapted with permission from Reference 41. Abbreviations: SHE, spin Hall effect; TR, time reversal.

Previous studies have almost exclusively been limited to nonmagnetic materials in which the spin Hall property is insensitive to the external magnetic fields. Namely, the conventional contribution is invariant under time reversal operation (134, 135).

In this context, a qualitatively new type of SHE may arise only in systems with broken TRS (41, 136, 137). The noncollinear antiferromagnet Mn_3Sn, in which TRS is macroscopically broken by the octupole order, is found to exhibit a new type of SHE (the MSHE) that is magnetically controllable. Namely, the spin accumulation vector generated by the SHE can be reversed when the direction of magnetic staggered moment is switched (**Figure 7**), indicating that the dominant contribution to the SHE is odd under time reversal (41, 127). This demonstrates that spin Hall

properties in noncollinear antiferromagnets are much richer than those in the commonly studied strongly spin-orbit-coupled paramagnetic metals. In addition, the MSHE induces out-of-plane spin accumulation and, thus, is useful to electrically switch the perpendicularly oriented magnetic moment under zero field (138). This may be related to the facet dependence of SOT found in another noncollinear antiferromagnet, Mn_3Ir (139).

3.7. Electrical Manipulation of a Weyl Semimetallic State

Electrical control of magnetization through spin-torques has enabled significant innovations, not only in the development of nonvolatile memories but also in basic spintronics research using ferromagnets and antiferromagnets (31–34, 83, 133, 141–145). In fact, the recent intensive studies have led to the breakthrough of the electric-current control of AF sublattices and its detection using AMR or spin Hall magnetoresistance (SMR) (88, 146–149). However, contrary to conventional FM spintronics, these emerging technologies operate on more complicated terminal schemes and/or configurations, because a single bidirectional current is not enough to detect and/or control the binary states with different axes of AF sublattice (88, 146–149). Thus, additional operation schemes are required to apply current along different directions with respect to the crystalline axes, hampering the integration to conventional spintronics. To simply replace an antiferromagnet as the active element, we need to select a useful material that allows us to employ the same protocol developed for the conventional spintronics. For instance, it would be beneficial to use TR odd responses (linear in magnetization $\boldsymbol{M}$) for the readout, such as AHEs and Faraday/Kerr effects as found in Mn_3Sn, in comparison with the TR-even (quadratic in $\boldsymbol{M}$) responses frequently used to detect an AF state (e.g., AMR, quadratic magneto-optical effects) (31, 32, 34, 89, 150). Such an $\boldsymbol{M}$-linear response may appear as a direct consequence of the reversal of AF sublattice moments and should not be obscured by current-induced nonmagnetic effects (151). Furthermore, if we could apply a deterministic switching scheme using bidirectional electrical current, the same protocol as the one used for conventional spintronics, namely, the combination of bidirectional-current-induced switching and the readout by the $\boldsymbol{M}$-linear-response may well become available to develop AF spintronics devices.

In this context, the recent observation of deterministic switching of topological antiferromagnetism in Mn_3Sn by bidirectional electric current and its detection by AHE is significant (**Figure 8*a***). In sharp contrast with previous studies in which epitaxial films are essential for SOT switching in antiferromagnets, polycrystalline thin film of Mn_3Sn fabricated on Si/SiO_2 substrate was utilized to integrate the AF metal Mn_3Sn on the four-probe switching system using a Hall bar (**Figure 8*b***; 121). Using the bilayer device made of Mn_3Sn and nonmagnetic metals (NMs), it was found that an electrical current with the density of 10^{10}–10^{11} A/m^2 in NMs induces a magnetic switching, leading to a large change in the Hall voltage (**Figure 8*c***). In addition, the polarity of the electrical current along a bias field and the sign of the spin Hall angle θ_{SH} of NMs [Pt ($\theta_{SH} > 0$), Cu($\theta_{SH} \sim 0$) and W($\theta_{SH} < 0$)] determines the switching direction. Namely, the device with a Pt thin film shows opposite polarity to one with a thin film of W. The switching size is found to be nearly zero for the case of the bilayer device with Cu. In addition, the size of the switching Hall voltage was found to be magnified by several times through annealing after deposition of the heavy metal to change the interfacial condition (90). The demonstration of the deterministic electrical switching in an antiferromagnet using the same protocol as that used for ferromagnets such as Py and CoFe(B) is significant. It has also been reported that the pulse current creates and drives the AF domain walls owing to octupoles along a wire made of Mn_3Sn (152). These may well lead to another leap in science and technology of AF spintronics and topological magnets.

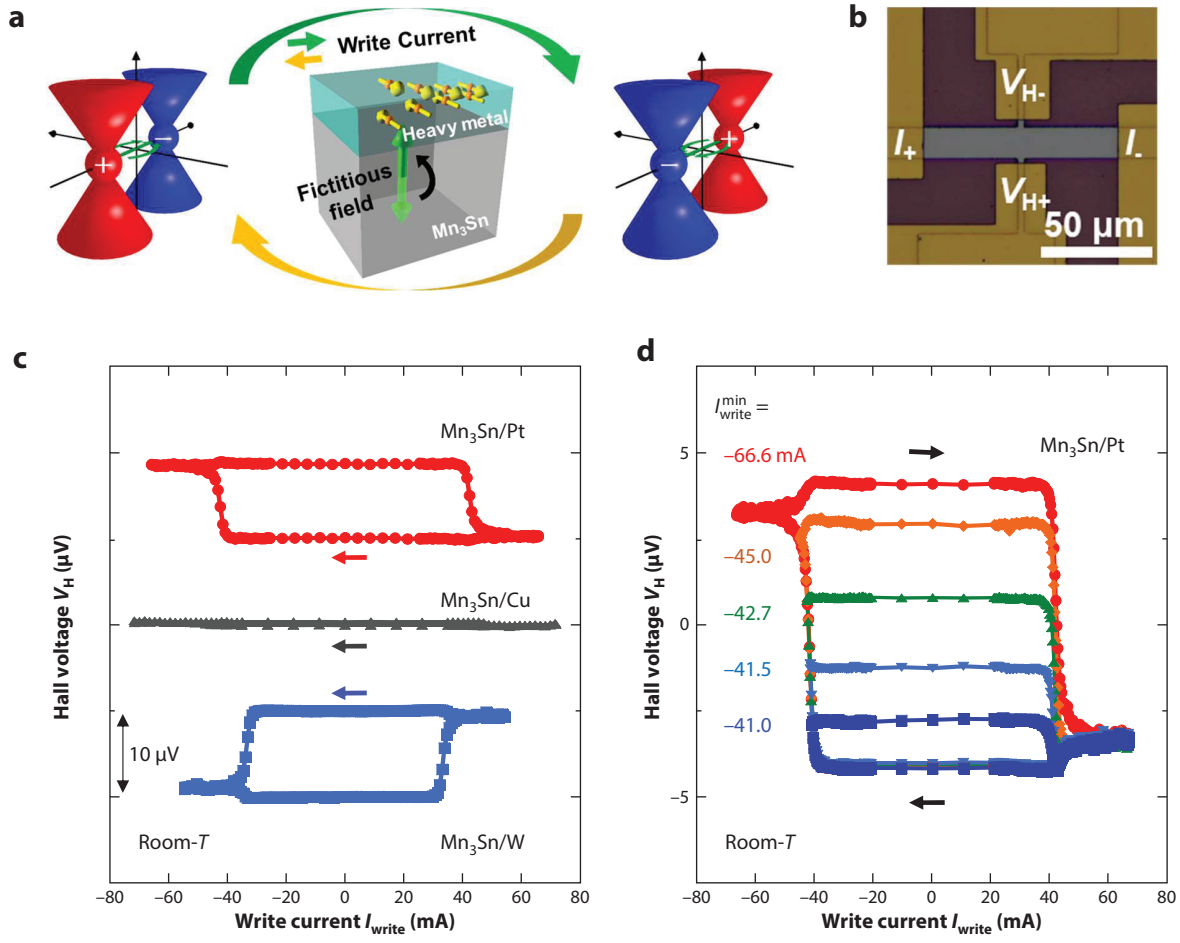

Figure 8

Electrical manipulation of the antiferromagnetic Weyl semimetallic state of Mn_3Sn at room temperature (see 43, 90, 140). (*a*) Schematic illustration for the electrical switching of the Weyl semimetal state. The polarity of the magnetic charge at the Weyl points and the associated Berry curvature or fictitious field is reversed by electrical switching. (*b*) Hall device using Mn_3Sn (*gray*). (*c*) Write current I_{write} dependence of the Hall voltage V_H for Mn_3Sn/Tr (Tr = Pt, Cu, W) devices. (*d*) Analog response. V_H–I_{write} loops for the Mn_3Sn/Pt device with various minimum write current I^{min}_{write}. Figure adapted with permission from Reference 43.

4. FERROMAGNETIC NODAL-LINE SEMIMETAL AND THERMOELECTRIC TECHNOLOGY

Today, for powering trillions of IoT sensors and wearable devices, there are growing demands for novel energy-harvesting technologies instead of batteries, in particular in the form of flexible, durable microthermoelectric generators (μ-TEGs). Thermoelectric power generation is one of the most ecological methods for generating electricity from waste or environmental heat because it can directly convert thermal energy to electric energy without any mechanical and chemical processes. Thus, the Seebeck effect has been intensively studied for a long time (153). However, the practical application using the thermopile based on the conventional Seebeck effect faces a number of difficulties such as very high production costs (for the complicated pillars of alternating

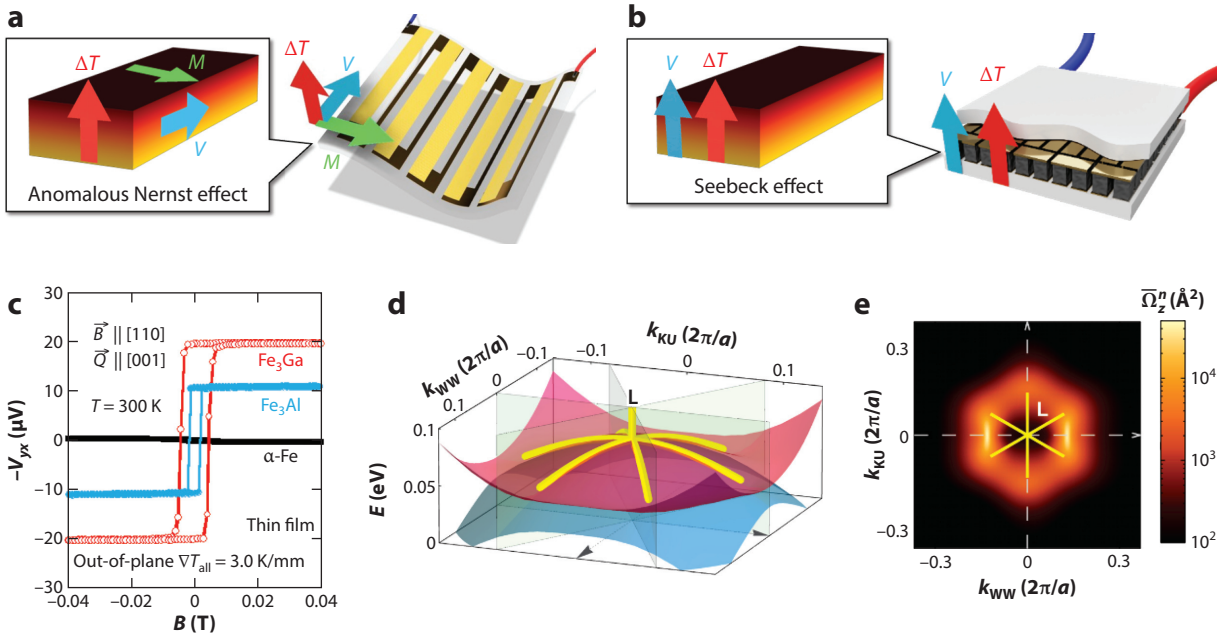

Figure 9

Thermoelectric modules using ANEs and Seebeck effects, and a giant ANE found in the nodal-line semimetal Fe_3X, X = Ga, Al. The orthogonal relation between the electric field and heat current for the ANE enables a lateral configuration of the thermoelectric modules to efficiently cover a heat source even with a curved surface (*a*). However, as the Seebeck effect generates the electric field parallel to the applied heat current, the thermopile needs to have the complicated pillar structure of alternating P and N type semiconductors (*b*). (*c*) Field dependence of the transverse voltage for Fe_3Ga, Fe_3Al, and α-Fe thin films. (*d*) Nodal web structure: two Fermi pockets (*red* and *blue curvature*) touching around L point along nodal lines (*yellow lines*). (*e*) Contour map of the Berry curvature enhanced around the nodal web (*yellow lines*). Figure adapted with permission from Reference 37. Abbreviation: ANE, anomalous Nernst effect.

S- and N-type semiconductors and a great number of contacts) and the usage of the rare, toxic, and brittle elements such as Bi, Pb, and Te (**Figure 9*b***).

Recently, another type of thermoelectric conversion, the ANE, has attracted significant attention as the next-generation technology: Its transverse geometry allows efficient, large area, and flexible coverage of a curved heat source with a much lower production cost (much simpler structure) (**Figure 9*a***; 11, 35–37, 39, 154–156). The reason behind the recent trend is a series of discoveries made in the field of topological magnets, as discussed in Section 2. Breaking the conventional wisdom, namely, that the ANE is proportional to magnetization and observed only in ferromagnets, the recent discovery of Weyl magnets has shown that topological magnets may exhibit much larger ANEs than those expected by the conventional scaling law, and even antiferromagnets may exhibit a large ANE such that its size is equivalent to those in ferromagnets (**Figure 1*b***; Section 3.4). This indicates that the large enhancement in Berry curvature may lead to strongly enhanced ANEs.

Following this stream of research, the successful application of the high-throughput search has been conducted for the two-body quantities, the anomalous Hall and thermoelectric coefficients (37). In particular, iron-based compounds have been investigated, as iron is not only a safe, popular element but the most naturally abundant and the lowest in cost. The search has produced a list of 1,400 candidate materials, and subsequent experiment has discovered the large transverse

thermoelectric effect in the iron-based compound Fe_3Ga, and Fe_3Al. The size of the ANE at room temperature ~6 μV/K is close to the highest record known to date (11), and the transverse thermoelectric coefficient reaches the maximum value of 5.5 A/Km (37). The discovery of the large ANE in naturally abundant elements is significant because it has the potential to reduce the production cost of thermopiles by two to three orders of magnitude, enabling the design of low-cost energy harvesters for IoT sensors and wearable devices. In addition, some thin films were successfully fabricated and exhibited the largest ANEs among the reports for films (**Figure 9*c***). This may well be the key technology for producing flexible thermopiles as well as for future spintronics applications.

Furthermore, experiment and theory have revealed a significant role for a nodal-line semimetal state in enhancing the transverse thermoelectric effect (**Figure 9*d***). Namely, the large ANE comes from Berry curvature enhanced around the nodal web, a flat band made of an interconnected nodal-line structure (**Figure 9*d*,*e***). Recently, Minami et al. have shown that there is a clear one-to-one correspondence between the DOS of the nodal line and the Fermi-energy dependence of the thermoelectric conductivity (157). Whereas the DOS of a nodal line diverges at stationary points, the thermoelectric conductivity also diverges when the Fermi energy coincides with the energy of the stationary points. Together with the nodal-point semimetal, the nodal web semimetal would be a concept useful for materials design of next-generation thermoelectric materials.

5. CONCLUSION AND PERSPECTIVES

Since the discovery of electromagnetism, external magnetic fields produced by ferromagnets as well as electric currents have been essential for realizing motors and power generation. Internal magnetic fields due to magnetic moments in ferromagnets, however, induce spin-polarized current and spin current, serving as the basis of memories and sensors in today's spintronics. In contrast, the discovery of large transverse responses in topological magnets, such as the AHE in antiferromagnets, is based on the fictitious fields or Berry curvature coming from the quantum Berry phase of electronic wave function, rather than the external magnetic fields and the magnetization of ferromagnets.

As a highlight of the rapidly developing field of topological magnets, we reviewed recent studies of the topological antiferromagnet Mn_3Sn. It has been unveiled that the fictitious field may be equivalent to the external magnetic field of a few hundred tesla, and when it couples with electric current, the antiferromagnet exhibits the large AHE that exceeds those in ferromagnets (9, 28, 29). When it couples with heat current and light, the antiferromagnet shows the ANE (35) and magneto-optical effects (40, 42, 158), respectively, again with a large size comparable with or exceeding those in ferromagnets. Furthermore, it has been shown that magnetic Weyl particles are the origin of the large fictitious fields (10, 30). It is an interesting subject to clarify how they are related to the novel spintronic phenomena such as the MSHE found in the topological antiferromagnet (41, 136–138).

The discovery of the magnetic Weyl fermions opens up a research field for the new type of magnet, the Weyl magnet, in material science and spintronics. In sharp contrast with conventional ones, the Weyl antiferromagnets such as Mn_3Sn not only exhibit the large transverse responses at room temperatures but carry cluster magnetic octupoles in their magnetic texture that makes such responses controllable by a weak magnetic field and electric current. These striking properties have further sparked the in-depth fundamental research on novel topological and emergent electromagnetic phenomena due to magnetic Weyl fermions in the bulk and the surface/interfaces, laying the foundation for topological AF spintronics that will develop into future technologies including low-power and ultrafast nonvolatile memory and logic circuits.

More generally, the nontrivial topology of the electronic band structure coming from nodal points and nodal lines is very important to designing functionalities such as thermoelectric properties. In fact, the giant ANEs found in the FM Weyl and nodal-line semimetals (11, 37) make it realistic to design a new type of heat current sensors and thermoelectric generators using much simpler configurations than the conventional counterpart based on the Seebeck effect. The study of topological properties in the bulk and interfaces of correlated materials has just been initiated, and more exotic phenomena and useful technologies will surely be seen in the near future.

DISCLOSURE STATEMENT

The authors are not aware of any affiliations, memberships, funding, or financial holdings that might be perceived as affecting the objectivity of this review.

ACKNOWLEDGMENTS

We thank Akito Sakai, Tomoya Higo, Takahiro Tomita, and Ming Fu for their comments and contributions. We also thank for collaboration the group members of YoshiChika Otani, Shinji Miwa, Kei Yakushiji, Kouta Kondou, Collin Broholm, Peter Armitage, Hua Chen, Allan MacDonald, Robert D. Shull, and Joseph Orenstein. We also acknowledge Motoaki Hirayama, Marie-Therese Huebsch, Fumiyuki Ishii, Motoharu Kitatani, Takashi Koretsune, Susumu Minami, Takuya Nomoto, Masayuki Ochi, Shiro Sakai, and Michi-To Suzuki for their contributions. This work is partially supported by JST-CREST (JPMJCR18T3), JST-Mirai Program (JPMJMI20A1) and Grants-in-Aid for Scientific Research (19H00650). Institute for Quantum Matter, an Energy Frontier Research Center, was funded by DOE, Office of Science, Basic Energy Sciences under Award DE-SC0019331.

LITERATURE CITED

1. Castro Neto AH, Guinea F, Peres N, Novoselov KS, Geim AK. 2009. *Rev. Mod. Phys.* 81(1):109–62
2. Hasan MZ, Kane CL. 2010. *Rev. Mod. Phys.* 82(1):3045–67
3. Ando Y. 2013. *J. Phys. Soc. Jpn.* 82(1):102001
4. Machida Y, Nakatsuji S, Onoda S, Tayama T, Sakakibara T. 2010. *Nature* 463(7278):210–13
5. Yan B, Felser C. 2017. *Annu. Rev. Condens. Matter Phys.* 8(1):337–54
6. Armitage NP, Mele EJ, Vishwanath A. 2018. *Rev. Mod. Phys.* 90(1):015001
7. Wan X, Turner AM, Vishwanath A, Savrasov SY. 2011. *Phys. Rev. B* 83(20):205101
8. Burkov AA, Balents L. 2011. *Phys. Rev. Lett.* 107(12):127205
9. Nakatsuji S, Kiyohara N, Higo T. 2015. *Nature* 527(7577):212–15
10. Kuroda K, Tomita T, Suzuki MT, Bareille C, Nugroho AA, et al. 2017. *Nat. Mater.* 16(11):1090–95
11. Sakai A, Mizuta YP, Nugroho AA, Sihombing R, Koretsune T, et al. 2018. *Nat. Phys.* 14:1119–24
12. Liu E, Sun Y, Kumar N, Muechler L, Sun A, et al. 2018. *Nat. Phys.* 14(11):1125–31
13. Belopolski I, Manna K, Sanchez DS, Chang G, Ernst B, et al. 2019. *Science* 365(6459):1278–81
14. Liu DF, Liang AJ, Liu EK, Xu QN, Li YW, et al. 2019. *Science* 365(6459):1282–85
15. Fert A, Cros V, Sampaio J. 2013. *Nat. Nanotechnol.* 8:152–56
16. Nagaosa N, Tokura Y. 2013. *Nat. Nanotechnol.* 8:899–911
17. Yang SH, Naaman R, Paltiel Y, Parkin SSP. 2021. *Nat. Rev. Phys.* 3:328–343
18. Balents L. 2010. *Nature* 464(7286):199–208
19. Rau JG, Gingras MJ. 2019. *Annu. Rev. Condens. Matter Phys.* 10:357–86
20. Broholm C, Cava RJ, Kivelson SA, Nocera DG, Norman MR, Senthil T. 2020. *Science* 367(6475):eaay0668
21. Witczak-Krempa W, Chen G, Kim YB, Balents L. 2014. *Annu. Rev. Condens. Matter Phys.* 5(1):57–82
22. Takagi H, Takayama T, Jackeli G, Khaliullin G, Nagler SE. 2019. *Nat. Rev. Phys.* 1(4):264–80

23. Dzero M, Sun K, Galitski V, Coleman P. 2010. *Phys. Rev. Lett.* 104(10):106408
24. Lai HH, Grefe SE, Paschen S, Si Q. 2018. *PNAS* 115(1):93–97
25. Ye L, Kang M, Liu J, von Cube F, Wicker CR, et al. 2018. *Nature* 555:638–42
26. Yin JX, Ma W, Cochran TA, Xu X, Zhang SS, et al. 2020. *Nature* 583(7817):533–36
27. Kang M, Ye L, Fang S, You JS, Levitan A, et al. 2020. *Nat. Mater.* 19(2):163–69
28. Kiyohara N, Tomita T, Nakatsuji S. 2016. *Phys. Rev. Appl.* 5(6):064009
29. Nayak AK, Fischer JE, Sun Y, Yan B, Karel J, et al. 2016. *Sci. Adv.* 2(4):e1501870
30. Chen T, Tomita T, Minami S, Fu M, Koretsune T, et al. 2021. *Nat. Comm.* 12:572
31. Jungwirth T, Marti X, Wadley P, Wunderlich J. 2016. *Nat. Nanotech.* 11(1):231–41
32. Baltz V, Manchon A, Tsoi M, Moriyama T, Ono T, Tserkovnyak Y. 2018. *Rev. Mod. Phys.* 90(1):015005
33. Šmejkal L, Mokrousov Y, Yan B, MacDonald AH. 2018. *Nat. Phys.* 14:242–51
34. Bonbien V, Zhuo F, Salimath A, Ly O, Abbout A, Manchon A. 2021. arXiv:2102.01632
35. Ikhlas M, Tomita T, Koretsune T, Suzuki MT, Nishio-Hamane D, et al. 2017. *Nat. Phys.* 13(11):1085–90
36. Guin SN, Vir P, Zhang Y, Kumar N, Watzman SJ, et al. 2019. *Adv. Mater.* 31(25):1806622
37. Sakai A, Minami S, Koretsune T, Chen T, Higo T, et al. 2020. *Nature* 581(1):53–57
38. Goswami P, Tewari S. 2013. *Phys. Rev. B* 88(24):245107
39. Mizuguchi M, Nakatsuji S. 2019. *Sci. Tech. Adv. Mater.* 20(1):262–75
40. Higo T, Man H, Gopman DB, Wu L, Koretsune T, et al. 2018. *Nat. Photon.* 12(2):73–78
41. Kimata M, Chen H, Kondou K, Sugimoto S, Muduli PK, et al. 2019. *Nature* 565(7741):627–30
42. Matsuda T, Kanda N, Higo T, Armitage NP, Nakatsuji S, Matsunaga R. 2020. *Nat. Commun.* 11(8):909
43. Tsai H, Higo T, Kondou K, Nomoto T, Sakai A, et al. 2020. *Nature* 580(0):608–13
44. Otani Y, Higo T. 2021. *Appl. Phys. Lett.* 118(4):040501
45. Yang KY, Lu YM, Ran Y. 2011. *Phys. Rev. B* 84(7):075129
46. Chen H, Niu Q, MacDonald AH. 2014. *Phys. Rev. Lett.* 112(1):017205
47. Kübler J, Felser C. 2014. *Euro. Phys. Lett.* 108(6):67001
48. Yang H, Sun Y, Zhang Y, Shi WJ, Parkin SSP, Yan BH. 2017. *N. J. Phys.* 19:015008
49. Guo GY, Wang TC. 2017. *Phys. Rev. B* 96(22):224415
50. Zhang Y, Sun Y, Yang H, Železný J, Parkin SPP, et al. 2017. *Phys. Rev. B* 95(7):075128
51. Kübler J, Felser C. 2017. *Euro. Phys. Lett.* 120(4):47002
52. Nagaosa N, Sinova J, Onoda S, MacDonald AH, Ong NP. 2010. *Rev. Mod. Phys.* 1(1):1539–92
53. Xiao D, Chang MC, Niu Q. 2010. *Rev. Mod. Phys.* 82(3):1959–2007
54. Karplus R, Luttinger JM. 1954. *Phys. Rev.* 95(5):1154–60
55. Weyl H. 1929. *Z. Phys.* 56(1):330–52
56. Xu SY, Belopolski I, Alidoust N, Neupane M, Bian G, et al. 2015. *Science* 349(6248):613–17
57. Lv BQ, Weng HM, Fu BB, Wang XP, Miao H, et al. 2015. *Phys. Rev. X* 5(3):031013
58. Ali MN, Xiong J, Flynn S, Tao J, Gibson QD, et al. 2014. *Nature* 514(7521):205–8
59. Nielsen HB, Ninomiya M. 1983. *Phys. Lett. B* 130(6):389–96
60. Son DT, Spivak BZ. 2013. *Phys. Rev. B* 88(10):104412
61. Nakatsuji S, Machida Y, Maeno Y, Tayama T, Sakakibara T, et al. 2006. *Phys. Rev. Lett.* 96(8):087204
62. Balicas L, Nakatsuji S, Machida Y, Onoda S. 2011. *Phys. Rev. Lett.* 106(21):217204
63. Lee WL, Watauchi S, Miller VL, Cava RJ, Ong NP. 2004. *Phys. Rev. Lett.* 93(22):226601
64. Miyasato T, Abe N, Fujii T, Asamitsu A, Onose Y, et al. 2007. *J. Magn. Magn. Mater.* 310(2):1053–55
65. Xiao D, Yao Y, Fang Z, Niu Q. 2006. *Phys. Rev. Lett.* 97(2):026603
66. Smith AW. 1911. *Phys. Rev. (Series I)* 33(4):295–306
67. Li X, Xu L, Ding L, Wang J, Shen M, et al. 2017. *Phys. Rev. Lett.* 119(5):056601
68. Soluyanov AA, Gresch D, Wang ZJ, Wu QS, Troyer M, et al. 2015. *Nature* 527(7579):495–98
69. Guin SN, Manna K, Noky J, Watzman SJ, Fu C, et al. 2019. *NPG Asia Mater.* 11:16
70. Xu L, Li X, Ding L, Chen T, Sakai A, et al. 2020. *Phys. Rev. B* 101(18):180404
71. Sumida K, Sakuraba Y, Masuda K, Kono T, Kakoki M, et al. 2020. *Commun. Mater.* 1:89
72. Kleiner WH. 1966. *Phys. Rev.* 142(2):318–26
73. Kleiner WH. 1967. *Phys. Rev.* 153(3):726–27
74. Kleiner WH. 1969. *Phys. Rev.* 182(3):705–9

75. Seemann M, Ködderitzsch D, Wimmer S, Ebert H. 2015. *Phys. Rev. B* 92(15):155138
76. Kuramoto Y, Kusunose H, Kiss A. 2009. *J. Phys. Soc. Jpn.* 78:072001
77. Santini P, Carretta S, Amoretti G, Caciuffo R, Magnani N, Lander GH. 2009. *Rev. Mod. Phys.* 81(2):807–63
78. Mydosh JA, Oppeneer PM, Riseborough PS. 2020. *J. Phys. Condens. Matter* 32(14):143002
79. Suzuki MT, Koretsune T, Ochi M, Arita R. 2017. *Phys. Rev. B* 95(9):094406
80. Suzuki MT, Nomoto T, Arita R, Yanagi Y, Hayami S, Kusunose H. 2019. *Phys. Rev. B* 99(17):174407
81. Nomoto T, Arita R. 2020. *Phys. Rev. Res.* 2:012045(R)
82. Huebsch MT, Nomoto T, Suzuki MT, Arita R. 2021. *Phys. Rev. X* 11(1):011031
83. Chappert C, Fert A, Van Dau FN. 2007. *Nat. Mater.* 6(11):813–23
84. Shull CG, Samuel Smart J. 1949. *Phys. Rev.* 76(1):1256–57
85. Núñez AS, Duine RA, Haney P, MacDonald AH. 2006. *Phys. Rev. B* 73(21):214426
86. Gomonay EV, Loktev VM. 2014. *Low Temp. Phys.* 40(1):17–35
87. Higo T, Li Y, Kondou K, Qu D, Ikhlas M, et al. 2021. *Adv. Funct. Mater.* 31(15):2008971
88. Wadley P, Howells B, Železny J, Andrews C, Hills V, et al. 2016. *Science* 351(6273):587–90
89. Marti X, Fina I, Frontera C, Liu J, Wadley P, et al. 2014. *Nat. Mater.* 13:367–74
90. Tsai H, Higo T, Kondou K, Sakamoto S, Kobayashi A, et al. 2021. *Small Sci.* 1(5):2000025
91. Chien CL, Westgate CR, eds. 1980. *The Hall Effect and Its Applications*. New York: Springer Sci. & Bus. Media
92. Hall EH. 1880. *Proc. Phys. Soc. Lond.* 4(1):325–42
93. Shindou R, Nagaosa N. 2001. *Phys. Rev. Lett.* 87(11):116801
94. Martin I, Batista CD. 2008. *Phys. Rev. Lett.* 101(15):156402
95. Nagamiya T, Tomiyoshi S, Yamaguchi Y. 1982. *Solid State Commun.* 42(5):385–88
96. Tomiyoshi S, Yamaguchi Y. 1982. *J. Phys. Soc. Jpn.* 51(8):2478–86
97. Brown PJ, Nunez V, Tasset F, Forsyth JB, Radhakrishna P. 1990. *J. Phys. Condens. Matter.* 2(47):9409–22
98. Tomiyoshi S, Yamaguchi Y, Nagamiya T. 1983. *J. Magn. Magn. Mater.* 31-34:629–30
99. Yang SY, Wang Y, Ortiz BR, Liu D, Gayles J, et al. 2020. *Sci. Adv.* 6(31):eabb6003
100. Pippard AB. 1989. *Magnetoresistance in Metals*, Vol. 2. New York: Cambridge Univ. Press
101. Xiong J, Kushwaha SK, Liang T, Krizan JW, Hirschberger M, et al. 2015. *Science* 350(6259):413–16
102. Huang XC, Zhao LX, Long YJ, Wang PP, Chen D, et al. 2015. *Phys. Rev. X* 5(3):031023
103. Hirschberger M, Kushwaha S, Wang Z, Gibson Q, Liang S, et al. 2016. *Nat. Mater.* 15(11):1161–65
104. Haubold E, Koepernik K, Efremov D, Khim S, Fedorov A, et al. 2017. *Phys. Rev. B* 95(24):241108
105. Li X, Xu L, Zuo H, Subedi A, Zhu Z, Behnia K. 2018. *SciPost Phys.* 5(6):063
106. Xu L, Li X, Lu X, Collignon C, Fu H, et al. 2020. *Sci. Adv.* 6(17):eaaz3522
107. Sugii K, Imai Y, Shimozawa M, Ikhlas M, Kiyohara N, et al. 2019. arXiv:1902.06601
108. Wuttke C, Caglieris F, Sykora S, Scaravaggi F, Wolter AUB, et al. 2019. *Phys. Rev. B* 100(8):085111
109. Reichlova H, Janda T, Godinho J, Markou A, Kriegner D, et al. 2019. *Nat. Commun.* 10:5459
110. Miwa S, Iihama S, Nomoto T, Tomita T, Higo T, et al. 2021. *Small Sci.* 1:2000062
111. Liu J, Balents L. 2017. *Phys. Rev. Lett.* 119(8):087202
112. Li X, Collignon C, Xu L, Zuo H, Cavanna A, et al. 2019. *Nat. Commun.* 10(1):3021
113. Mansuripur M. 1995. *The Physical Principles of Magneto-optical Recording*. New York: Cambridge Univ. Press
114. Oppeneer PM. 1887. In *Handbook of Magnetic Materials*, Vol. 13, ed. KHJ Buschow, pp. 229–422. Amsterdam: Elsevier
115. McCord J. 2015. *J. Phys. D: Appl. Phys.* 48(1):333001
116. Feng W, Guo GY, Zhou J, Yao Y, Niu Q. 2015. *Phys. Rev. B* 92(14):144426
117. Wu M, Isshiki H, Chen T, Higo T, Nakatsuji S, Otani Y. 2020. *Appl. Phys. Lett.* 116(13):132408
118. Yamasaki Y, Nakao H, Arima T. 2020. *J. Phys. Soc. Jpn.* 89(8):083703
119. Sasabe N, Kimata M, Nakamura T. 2021. *Phys. Rev. Lett.* 126(15):157402
120. Markou A, Taylor JM, Kalache A, Werner P, Parkin SSP, Felser C. 2018. *Phys. Rev. Mater.* 2(5):051001
121. Higo T, Qu D, Li Y, Chien CL, Otani Y, Nakatsuji S. 2018. *Appl. Phys. Lett.* 113(20):202402
122. Ikeda T, Tsunoda M, Oogane M, Oh S, Morita T, Ando Y. 2018. *Appl. Phys. Lett.* 113(22):222405

123. Yoon J, Takeuchi Y, Itoh R, Kanai S, Fukami S, Ohno H. 2019. *Appl. Phys. Express* 13(1):013001
124. You Y, Chen X, Zhou X, Gu Y, Zhang R, et al. 2019. *Adv. Electron. Mater.* 5(3):1800818
125. Taylor JM, Markou A, Lesne E, Sivakumar PK, Luo C, et al. 2020. *Phys. Rev. B* 101(9):094404
126. Nakano T, Higo T, Kobayashi A, Miwa S, Nakatsuji S, Yakushiji K. 2021. *Phys. Rev. Mater.* 5(5):054402
127. Muduli PK, Higo T, Nishikawa T, Qu D, Isshiki H, et al. 2019. *Phys. Rev. B* 99(18):184425
128. Hirsch JE. 1999. *Phys. Rev. Lett.* 83(9):1834–37
129. Kato YK, Myers RC, Gossard AC, Awschalom DD. 2004. *Science* 306(5703):1910–13
130. Wunderlich J, Kaestner B, Sinova J, Jungwirth T. 2005. *Phys. Rev. Lett.* 94(4):047204
131. Saitoh E, Ueda M, Miyajima H, Tatara G. 2006. *Appl. Phys. Lett.* 88(18):182509
132. Kimura T, Otani Y, Sato T, Takahashi S, Maekawa S. 2007. *Phys. Rev. Lett.* 98(15):156601
133. Liu L, Pai CF, Li Y, Tseng HW, Ralph DC, Buhrman RA. 2012. *Science* 336(0):555–58
134. Sinova J, Valenzuela SO, Wunderlich J, Back CH, Jungwirth T. 2015. *Rev. Mod. Phys.* 87(4):1213–60
135. Hellman F, Hoffmann A, Tserkovnyak Y, Beach GSD, Fullerton EE, et al. 2017. *Rev. Mod. Phys.* 89(2):025006
136. Železný J, Zhang Y, Felser C, Yan B. 2017. *Phys. Rev. Lett.* 119(18):187204
137. Nan T, Quintela CX, Irwin J, Gurung G, Shao DF, et al. 2020. *Nat. Commun.* 11(1):4671
138. Chen X, Shi S, Shi G, Fan X, Song C, et al. 2021. *Nat. Mater.* 20(6):800–4
139. Zhang W, Han W, Yang SH, Sun Y, Zhang Y, et al. 2016. *Sci. Adv.* 2(9):e1600759
140. Tsai H, Higo T, Kondou K, Kobayashi A, Nakano T, et al. 2021. *AIP Adv.* 11(4):045110
141. Slonczewski JC. 1996. *J. Magn. Magn. Mater.* 159(1–2):L1–7
142. Berger L. 1996. *Phys. Rev. B.* 54(1–2):9353
143. Katine JA, Albert FJ, Buhrman RA, Myers EB, Ralph DC. 2000. *Phys. Rev. Lett.* 84(1–2):3149
144. Miron IM, Garello K, Gaudin G, Zermatten PJ, Costache MV, et al. 2011. *Nature* 476:189–93
145. MacDonald AH, Tsoi M. 2011. *Philos. Trans. R. Soc. A* 369(1948):3098–114
146. Bodnar S, Šmejkal YL, Turek I, Jungwirth T, Gomonay O, et al. 2018. *Nat. Commun.* 9:348
147. Moriyama T, Oda K, Ohkochi T, Kimata M, Ono T. 2018. *Sci. Rep.* 8:14167
148. Chen XZ, Zarzuela R, Zhang J, Song C, Zhou XF, et al. 2018. *Phys. Rev. Lett.* 120:207204–6
149. Zhou X, Chen X, Zhang J, Li F, Shi G, et al. 2019. *Phys. Rev. Appl.* 11(5):054030
150. Saidl V, Němec P, Wadley P, Hills V, Campion RP, et al. 2017. *Nat. Photon.* 11(5):91–96
151. Chiang CC, Huang SY, Qu D, Wu PH, Chien CL. 2019. *Phys. Rev. Lett.* 123(22):227203
152. Sugimoto S, Nakatani Y, Yamane Y, Ikhlas M, Kondou K, et al. 2020. *Commun. Phys.* 3:111
153. Bell LE. 2008. *Science* 321(5895):1457–61
154. Sakuraba Y, Hasegawa K, Mizuguchi M, Kubota T, Mizukami S, et al. 2013. *Appl. Phys. Express* 6(3):033003
155. Narita H, Ikhlas M, Kimata M, Nugroho AA, Nakatsuji S, Otani Y. 2017. *Appl. Phys. Lett.* 111(20):202404
156. Li X, Zhu Z, Behnia K. 2021. *Adv. Mater.* 33(20):2100751
157. Minami S, Ishii F, Hirayama M, Nomoto T, Koretsune T, Arita R. 2020. *Phys. Rev. B* 102(20):205128
158. Kargarian M, Randeria M, Trivedi N. 2015. *Sci. Rep.* 5:12683